Université de Montréal

Volumetric Analysis of Plexiform Neurofibroma for Patients Treated with Trametinib

Par

Dorsa Sadat Kiaei

Département de pharmacologie et physiologie, Institut de génie biomédical

Faculté de médecine

Mémoire présenté en vue de l'obtention du grade de Maîtrise es sciences appliquées (M.sc.A.)
en génie biomédical

Aout 2022

© Dorsa Kiaei, 2022

Université de Montréal

Unité académique : Institut de génie biomédical, Faculté de médecine

Ce mémoire intitulé

Volumetric Analysis of Plexiform Neurofibroma for Patients Treated with Trametinib

Présenté par

Dorsa Sadat Kiaei

A été évalué par un jury composé des personnes suivantes

Alain Vinet, PhD
Président-rapporteur

Mathieu Dehaes, PhD
Directeur de recherche

Sébastien Perreault, MD
Codirectrice

Philippe Major, MD
Membre du jury

Résumé

Des recherches récentes suggèrent que le trametinib (inhibiteur de MEK) peut traiter les neurofibrome plexiforme (NP) provoquées par la neurofibromatose de type 1 (NF1). Les NP peuvent apparaître n'importe où dans le corps près des nerfs. Ces tumeurs se distinguent par leur forme inhabituelle et leur morphologie irrégulière qui les rendent difficile à mesurer.

Pour évaluer l'efficacité du trametinib dans le traitement des NP, nous suggérons une analyse volumétrique (mesure 3D) plutôt que des mesures 1D et 2D (habituelles) basées sur l'imagerie par résonance magnétique (IRM). Pour cette étude, des examens IRM ont été réalisés à des intervalles d'environ trois mois pour trente-quatre patients atteints de NP.

J'ai développé une méthode semi-automatique pour segmenter les PN sur les images IRM. J'ai testé et validé notre nouvelle approche et soumis un manuscrit incluant la description de la nouvelle méthodologie et les résultats de segmentation pour publication dans l'American Journal of Neuroradiology (AJNR). J'ai mis en place un outil pratique pour estimer avec précision le volume tumoral en utilisant cette méthode de segmentation. En conséquence, le suivi des changements tout au long du traitement devient possible et fiable.

L'analyse volumétrique réalisée chez 34 participants recrutés durant l'essai clinique révèle que le trametinib a entrainer une diminution du volume médian de la lésion initiale d'environ 20 % pour la période de 18 mois de traitement.

Mots-clés: Imagerie par résonance magnétique (IRM), Neurofibrome plexiforme (PN), Segmentation tissulaire, Analyse volumétrique, Traitement d'images.

Abstract

Recent research suggests that the medication trametinib can treat plexiform neurofibroma (PN) lesions associated with neurofibromatosis type 1 (NF1) disease. PNs can appear anywhere in the body near nerves. These tumors are distinct by their unusual shape and irregular morphology, which is difficult to assess.

For evaluating trametinib's effectiveness in treating PN, we suggest a volumetric analysis (3D measurement) rather than 1D and 2D measures (typical) based on magnetic resonance imaging (MRI). For this study, MRI scans were performed at about three-month intervals for thirty-four patients with PN.

I developed a semi-automatic method to segment PNs on MRI images. I tested and validated our new approach and submitted a manuscript with the description of the novel methodology and findings for publication in the American Journal of Neuroradiology (AJNR). I implemented a practical tool for accurately estimating tumor volume using this segmentation method. As a result, tracking lesion changes throughout the course of therapy becomes available.

The volumetric analysis performed on 34 patients enrolled in the clinical trial reveals that trametinib decreased the initial median lesion volume by around 20% for the period of 18 months of treatment.

Keywords: Magnetic resonance imaging (MRI), Plexiform neurofibroma (PN), Tissue segmentation, Volumetric analysis, Image processing.

Table of contents

List of Tables and Figures

Supplementary Figure 2. A, Histogram analysis of the circular ROI drawn in B, the original MRI image. Segmentation of the lesion area using: C, SSTMean, D, SSTMini, and E, Manual tracing.

List of acronyms and abbreviations

NF1	Neurofibromatosis type 1
PN	plexiform Neurofibroma
ADHD	attention-deficit/hyperactivity disorder
MPNST	malignant peripheral nerve sheath tumor
MRI	magnetic resonance imaging
CT	computed tomography
PET	positron emission tomography
WHO	world health organization
RECIST	response evaluation criteria in solid tumors
EORTC	European organization for research and treatment of cancer
H	Hydrogen atom
m	mass
B	magnetic moment of spins
B_0	external magnetic field
M_Z	Magnetization in Z-direction
NMV	net magnetization vector
RF	radiofrequency
NMR	nuclear magnetic resonance
DT	dynamic threshold
ROI	region of interest
CHUSJ	CHU Sainte-Justine
MCH	Montreal Children's Hospital
CHUQ	CHU de Québec-Université Laval
SickKids	The Hospital for Sick Children
IWK	IWK Health Centre
ACH	Alberta Children's Hospital
CWHC	British Columbia Children's Hospital
NSERC	natural sciences and engineering research council of Canada
FRQS	fonds de recherche du Québec – santé

To Saeed, Ramin, and Sepideh

Acknowledgments

I would first like to thank my research director Mathieu Dehaes, Ph.D., and my co-director Sébastien Perreault, MD, who supported and guided me throughout this master's project.

I would also like to thank Dr. Jean Claude Decarie, MD, and Guillaume Leblanc, who provided the necessary expertise for the data gathering.

I would also like to thank the members of the laboratory. Rasheda Chowdhury, PhD., Simon Brais-Brunet, Anurudhya Karthikeyan, and Maryam Heidarifard advised me during my study. Likewise, I thank Imen Benhmida for her technical assistance.

Finally, I would like to express my gratitude to my husband, father, and mother, who kindly supported me throughout my academic work, day and night.

Introduction

Neurofibromatosis type 1 (NF1) is a prevalent genetic disease linked to a high rate of malignancies in the central and peripheral nervous systems. Plexiform Neurofibroma (PN) are nerve sheath tumors involving multiple fascicles. Clinical trials are ongoing to find an effective treatment for PN [1].

Magnetic resonance imaging (MRI) technology is a medical imaging technique to analyze intricate internal structures of the body. PNs are diagnosed and assessed using MRI images using a variety of methods. As the standard, radiologists take a 1D measurement using a ruler directly from the image to estimate the size of PNs. This measurement limitation for PNs is important as these tumors have complex and irregular shapes. Continuation or discontinuation of treatment often depends on this measurement.

Volumetric methods to assess changes in tumors from MRI data are emerging and have been implemented on commercial platforms. These approaches necessitate high computation times related to the segmentation process and sometimes manual corrections when the segmentation process fails. A fast, reproducible, and accurate technique to assess complex and asymmetric tumor evolution is critical for clinical decision-making in clinical trials involving therapeutical assessment.

Objectives and research hypothesis

In this thesis, I propose to develop a new volumetric method to quantify PN lesions in 3D. I hypothesize that my volumetric method will allow accurate lesion quantification compared to the gold standard (manual tracing) with faster computation times. I also hypothesize that the thresholding approach used by my method is more accurate than the one from a previously published tool. To address these hypotheses, I propose the following specific aims:

Aim 1. Develop a semi-automatic segmentation technique based on mean image intensity thresholding (defined as SSTMean).

Aim 2. Compare the performance of SSTMean with a semi-automatic segmentation technique based on minimum image intensity thresholding (defined as SSTMini) that is similar to a previous approach. Also, compare the performances of the two techniques with manual tracing.

Additionally, I include preliminary data of the ongoing trial (TRAM-01) using trametinib for PN. I completed the quantification of lesion progression in 34 patients (out of 45). These preliminary data are available in Chapter 6, where I present the general discussion.

Thesis plan

This document is divided into six chapters. The first chapter introduces background and clinical information on the NF1 related to PN lesions. The second chapter covers the specifications of MRI images. These two chapters explain the theory of the research and the logic behind data gathering. The third chapter covers elements critical to the study and data processing. In particular, there is a detailed description of the algorithms and the approaches previously used to segment MRI images. The fourth chapter initiates a short foreword to facilitate reading the article in Chapter 5. The fifth chapter contains a manuscript submitted to the American Journal of Neuroradiology (AJNR, impact factor 4.966 in 2021, ranked 14 among top publications in Radiology and Medical Imaging). This manuscript details the proposed semi-automatic MRI segmentation steps that I developed for the volumetric analysis of PNs. The sixth chapter offers a general discussion, describes some limitations and suggests future technical improvements in the current processing algorithm. Also, a short showcase of preliminary results is gathered in this chapter. In the end, we conclude the thesis and list the cited references.

Chapter 1 – Description of the pathology

1.1 Neurofibromatosis

This section describes the specific lesions pertinent to this thesis and provides information about the genetic disease that causes those tumors.

1.1.1 Neurofibromatosis disease

Neurofibromatosis type 1 (NF1) is an autosomal dominant tumor predisposition syndrome affecting 1:3000 people. NF1 is a gene found on chromosome 17. The product of the NF1 gene (NF1 or Neurofibromin) acts as a GTPase-activating protein (GAP) for Ras. Loss of NF1 leads to an increase in the active form of RAS. Patients with NF1 have susceptibility to the development of a tumor, including plexiform neurofibroma (PN) and pilocytic astrocytoma.

1.1.2 Symptoms

Patients with NF1 typically show signs and symptoms during infancy and can include [2]:

(1) hyper pigmentated brown skin (cafe au lait macules): These benign lesions are typical of NF1. More than six café au lait macules suggest NF1. They frequently manifest at birth or in the first few years of life.

(2) Freckling (smaller than café au lait spots)in the groin or armpit region: Freckling often begins between the ages of 3 and 5.

(3) Hamartoma (Lisch nodules) on the iris of the eye. These benign nodules are lesions that do not affect eyesight.

(4) Neurofibromas are soft, pea-sized lumps that typically form in or beneath the skin.

5) Plexiform neurofibromas NF1's pathognomonic neurofibromas are slowly progressing tumors affecting peripheral nerves and spinal roots. These PNs, which affect 25 to 50% of NF1 patients, cause severe morbidity depending on their size and location [2].

(6) Bone anomalies: Bone abnormalities like scoliosis or a bow-legged lower leg can result from abnormal bone growth and a lack of bone mineral density.

(7) An optic nerve tumor (optic glioma): These tumors are almost uncommon in adults, and they typically start developing by age 3.

(8) Learning disabilities: Children with NF1 frequently experience minor cognitive impairment. There is often a particular learning deficiency, such as difficulty with reading or learning mathematics. Both speech delay and attention-deficit/hyperactivity disorder (ADHD) are widespread conditions.

1.2 Plexiform neurofibroma (PN)

Neurofibromas are heterogeneous tumors composed of Schwann cells, fibroblasts, perineural cells, vascular cells, and invading hematopoietic cells, which are predominantly degranulating mast cells [3].

PNs usually progress relentlessly during childhood, adolescence, and adulthood, causing lifelong disfigurement, disability, and mortality [4]. Often PNs compress cranial nerves and/or peripheral nerve roots at the vertebral column and create an array of morbidities, including paresthesia, paralysis, blindness, difficulty swallowing, drooling, sleeplessness, respiratory and gastrointestinal distress, and loss of bowel and bladder control. A PN can also transform into a malignant peripheral nerve sheath tumor (MPNST), a highly morbid, metastatic cancer that afflicts up to 10% of NF1 patients in their lifetime [3].

1.2.1 Surgical treatment

Historically, surgical resection was the only treatment approach to address PN. However, they are typically challenging to remove due to PNs' infiltrative nature and location. Furthermore, despite resection, most PN will continue to progress. In a single Center study [5], 74 of the 168 surgically removed PN tumors continued to grow. Younger age at diagnosis, subtotal tumor excision, and the location were related to a greater risk of progression after surgery.

1.3 MEK inhibitors

MEK inhibitors were initially designed and developed to treat tumors and melanoma (skin cancer). The effects of these drugs on the cancers connected to NF1 are still being investigated. In current studies, most patients who use MEK inhibitors have shown tumors to diminish (but not

disappear). Changes in the tumor frequently do not begin in NF1 patients on MEK inhibitors until the patient has taken the drug for several months. MEK inhibitors used in a clinical trial include [6]: Binimetinib, Cobimetinib, Mirdametinib, Selumetinib, and Trametinib; which Trametinib was used in the present study.

MEK inhibition has been investigated in treating individuals with widespread PN with NF1 following RAS pathway-targeted therapeutic studies. Selumetinib was utilized in phase 1 and phase 2 clinical studies in this group to treat young patients with otherwise incurable PN. Seventy percent of the patients had PN shrinkage. Additionally, several patients reported reduced pain and improved function [7].

Selumetinib's Phase 1 and Phase 2 clinical data in refractory PLGG show a sustained partial response in up to 40% of children with these tumors, which is promising [8].

Trametinib is a highly selective, reversible inhibitor of MEK1/2 activation and kinase activity. Phase 1 and pre-clinical studies show encouraging outcomes in a limited subset of kids with optic pathways or PN gliomas [9] Trametinib has also been demonstrated to be effective and tolerable in a small number of kids with LGG and melanoma without NF1 [10]. As a result, trametinib has gained popularity as a treatment option for kids with symptomatic PN and resistant progressive PLGG [11], [12]. A phase 2 Canadian clinical research assesses trametinib in kids with PN and LGG [13], [14].

1.4 Imaging of PN

Medical imaging is a technique and process that offers visual representations of a body's interior for use in clinical analysis and medical intervention. It demonstrates the function of certain organs or tissues [15]. Medical imaging tries to diagnose and treat diseases by exposing internal structures hidden by the skin and bones. The three primary medical image modalities are computed tomography (CT), magnetic resonance imaging (MRI), and positron emission tomography (PET) [16].

. Plexiform Neurofibromas (PNs) can be monitored with MRI to assess treatment response, find aggressive tumors before they become malignant, and analyze tumor changes with (MRI). PN is

characterized by asymmetric development and complex morphology, making it challenging to accurately evaluate tumor growth using one or bi-dimensional methods [17].

Typically, the response of solid tumors is assessed using the RECIST 1.1 criteria The Response Evaluation Criteria in Solid Tumors (RECIST) was created in 2000, They were created by the European Organization for Research and Treatment of Cancer (EORTC) to increase the accessibility of evaluation and decrease inflated response rates [16]. These criteria streamline earlier methods for evaluating responses that were founded on the notion that one-dimensional data (such as the biggest diameter) are equally valid as bi-dimensional data [18].

Clinical studies for cancer currently make the most significant use of the RECIST criteria. These methods lack reproducibility and ignore the three-dimensional information that more recent imaging techniques offer. Additionally, certain lesions have asymmetric growth patterns, making them unsuitable for several assessment techniques. Because of the large or atypically shaped tumor that develops along numerous branches of peripheral nerves, standard linear measurements are inappropriate.

The next chapter contains a short description of the theoretical concepts of MRI. These basics are necessary for a better understanding of the article presented in Chapter 5.

Chapter 2 – Magnetic resonance imaging (MRI)

2.1 MRI basics

MRI technology is a medical imaging tool used in radiology to examine detailed interior structures. MRI uses the property of nuclear magnetic resonance (NMR) to view the nuclei of atoms inside the body. It is used to scan every region of the body. Still, it is beneficial for tissues like the brain, muscle, connective tissue, and most cancers with a lot of hydrogen nuclei and minimal density contrast [15].

MRI devices employ a strong magnetic field to align the magnetization of hydrogen nuclei in the body and radio waves at a particular frequency to change that alignment over time. The spins of the nuclei realign with the static magnetic field when the radio wave transmission is shut off. This relaxation produces a radio frequency signal, which receiver coils detect. Varying tissue types have different relaxation times, which is a specific characteristic. The recorded data creates a three-dimensional gray-scale image of the scanned body part.

Compared to other medical imaging techniques like CT or X-rays, MRI provides a strong contrast between the different soft tissues of the body, making it especially effective in viewing the brain, muscles, the heart, and tumors. MRI does not utilize ionizing radiation, unlike CT scans or regular X-rays, and is typically a safe imaging modality. It is the preferred approach for non-invasive tumor evaluation. It is crucial in classifying and grading patients and preoperative evaluation, follow-up, and therapeutic management.

While CT has a robust spatial resolution, and the capacity to identify two different structures apart at an arbitrarily small distance, MRI has comparable resolution but significantly superior contrast resolution, the ability to distinguish the difference between two arbitrarily similar but not identical tissues.

2.1.1 The physics of MRI

Magnetic resonance (MR) is defined as the signal from the nuclei of hydrogen atoms (^1H) excited by magnetism which then is used for image generation. A Hydrogen atom comprises a nucleus

with a single proton and an electron circling it. So, Hydrogen is known as the proton, and in the MR context, only the proton is the contrast.

The proton has a positive charge and spins around itself. The spin is a fundamental characteristic of elementary particles, which always have the same magnitude and cannot be accelerated or decelerated. Two crucial characteristics of a spinning proton are:

(1) Mass (m): The proton, being a revolving mass about an axis, stays upstanding in this axis direction because of the conservation of angular momentum. This behavior is similar to the physics of a spinning cone mounted on a surface (see Figure 1). The orientation of the axis is not affected by the tilting of the mounting surface, so the rotation provides stability to the cone (defined as a gyroscope device).
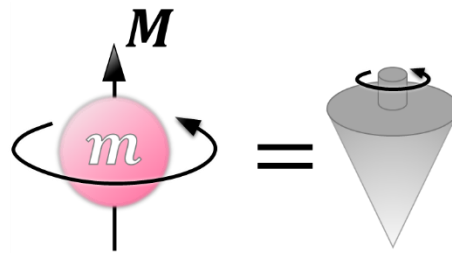
Figure 1. Proton spin characteristics as a mass

(2) Electrical charge (Positive charge): As a rotating electrical charge, the proton generates a small magnetic field (dipole), B. Simply put, it is a small magnet. So, in the presence of an external magnetic field (B_0), this magnet aligns with that field. Also, B_0 make the proton to orbit (wobble) while spinning. Like an electrical generator, this wobble creates a quantitatively detectable voltage in a receiver coil (see Figure 2).
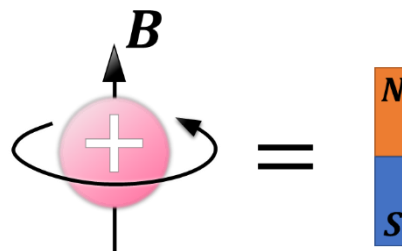
Figure 2. Proton spin characteristics as a positive electrical charge

A spinning cone starts wobbling when its energy is decayed by an external force (*e.g.*, friction). Precession is the term when that force makes the spin axis of that mass orbit. Similarly, the spin axis of a proton, which determines B direction, can wobble and be put into a precessional orbit (see Figure 3). Presenting B_0 near a proton is a decaying process since it creates the alignment of the spins (small magnets) parallel to that magnetic field. So, this energy dissipation makes protons start wobbling. The rate at which protons precess when put in an electromagnetic field is known as the Larmor frequency.
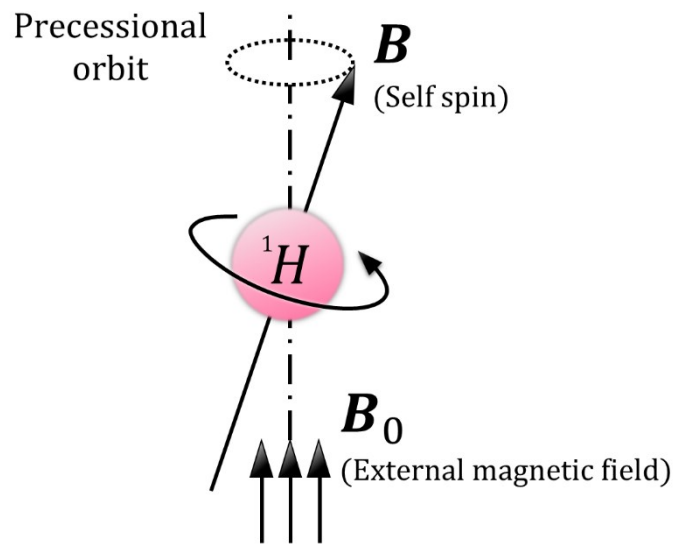
Figure 3. An external magnetic field can change spin direction.

The Larmor frequency refers to the typical speed of the nuclei's precession, which is proportional to the intensity of the applied magnetic field. The Larmor frequency is central in MRI basics and how scanners are built.

The human body mostly consists of water (H_2O), which contains hydrogen atoms. Powerful electromagnets of the MRI scanner excite hydrogen atoms of a particular slice of the body. This excitation has the returning signal from protons analyzed by a computer to make a user-readable image.

After the applied magnetic field along a patient's body (Z-direction) is removed, the spinning Hydrogen atom in the body relaxes and enters the previous stable state because the proton spin is a fundamental state always present and cannot become faster or slower. During relaxation,

longitudinal magnetization (in the Z-direction, denoted by M_Z) increases because the magnetic vectors corresponding to the individual magnetic moments add up. However, the resultant M_Z is very weak. For this reason, an MRI scanner's magnetic field B_0 has to be sufficiently stronger than the earth's magnetic field to measure a recognizable signal. In addition, this signal is collected with sensitive receivers and amplified.

2.1.2 T1 and T2 relaxation

The protons, which are typically randomly oriented inside the water nuclei of the tissue being investigated, are brought into alignment using a strong, uniform, external magnetic field B_0. The subsequent perturbation or disruption of this alignment (or magnetization) is caused by the addition of an external Radio Frequency (RF) energy. Through a variety of relaxation mechanisms, the nuclei return to their resting alignment and release RF energy in the process. The emitted signals are monitored after a certain amount of time has passed from the first RF. The signal from each place in the imaging plane is converted using the Fourier transform into the relevant intensity levels, which are then represented as shades of grey in a matrix of pixels.

Different kinds of images can be produced by altering the order in which RF pulses are delivered and collected. The interval between succeeding pulse sequences delivered to the same slice is known as the repetition time (TR). The period of time between the RF pulse being delivered and the echo signal received is known as the echo time (TE).

T1 and T2 are two separate relaxation durations that can be used to describe tissue. The time constant T1 (longitudinal relaxation time) controls how quickly excited protons return to equilibrium. It is an indicator of how long it takes for spinning protons to reorient themselves with the surrounding magnetic field. The time constant T2 (transverse relaxation time) controls how quickly excited protons attain equilibrium or shift out of phase with one another. It is a measurement of how long it takes for the nuclei spinning perpendicular to the main field to lose phase coherence among the spinning protons.

2.1.3 MRI planes

MR imaging generates cross-sectional images of the human body as a tomographic method. As a result, rather than applying the excitation pulse to the entire body, we only apply it to the slice we want to scan.

Anatomical coordinates are the standard model coordinate system for medical imaging. It is also called the patient coordinate system demonstrated in the following. While viewing MRI images in this coordinate system, the body's left side is displayed on the right. Simply put, the top-bottom and front-back locales are kept the same, but the sides are flipped.

2.1.3.1 Sagittal view

The sagittal plane (see Figure 4), also known as the median plane, is a y-z plane that divides left from right and is perpendicular to the ground. The unique sagittal plane that is precisely in the middle of the body is known as the mid-sagittal plane.
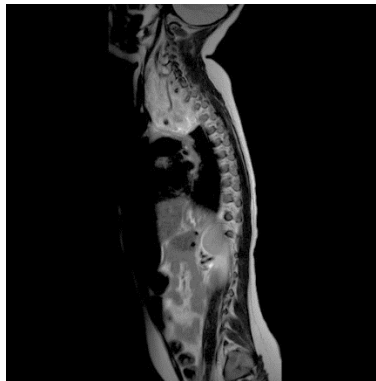
Figure 4. A sample MRI [19] slice in the sagittal axis

2.1.3.2 Coronal view

In humans, the anterior and posterior, front and back, and ventral and dorsal are separated by the coronal plane (see Figure 5), sometimes referred to as the frontal plane, which is an x-z plane perpendicular to the ground.
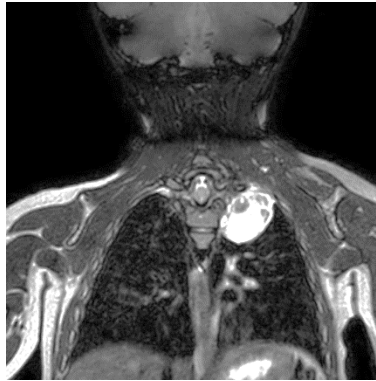
Figure 5. A sample MRI [19] slice in the coronal axis

2.1.3.3 Axial view

The transverse plane, often referred to as an axial plane (see Figure 6) or a horizontal plane, is an X, Y, and Z plane that is parallel to the ground and divides the superior from the inferior, or alternatively, the head from the feet, in humans.

Figure 6. A sample MRI [19] slice on the axial axis

Chapter 3 – MRI segmentation of tumors

3.1 MRI images used for segmentation

Here say that the following segmentation methods were mostly developed for STIR imaging. By suppressing the signals from fat and the combined effects of T1 and T2 processes on tissue brightening, the STIR approach employs an alternate MRI sequence. STIR imaging is a sensitive method for identifying tumors, edema, and infection in bone marrow [30].

3.2 Image segmentation

The spatial division of an image into its constituent pieces to isolate certain objects in an image is known as segmentation. Many segmentation approaches have been adopted to address a specific therapeutic requirement. Thresholding, clustering, region growth, edge-based approaches, deformable models, graph partitioning, and prior knowledge are among the methods discussed here. State-of-the-art segmentation algorithms [20] typically employ all these fundamental approaches as building elements.

3.2.1 Thresholding

This feature may be utilized to separate pixels that belong to an object and those that are not when a structure in the image is uniquely described by its intensity values. A gray-scale image is commonly used as the input to this approach. A single parameter known as the intensity threshold is set in basic implementations. The intensity threshold is applied to each pixel in the image. The result is a binary picture with ones where pixels meet the threshold criteria and zeroes where they don't. Manually or automatically, the threshold may be set based on picture statistics. For example, a local minimum in the image's intensity histogram might be used to differentiate between a bright object and its darker background.

Advanced techniques divide the picture into subsections, with each portion having a different threshold. This local thresholding aids in overcoming intensity shifts caused by magnetic field inhomogeneity in MRI scans or lighting variances in natural pictures. Thresholding's main benefit is its speed since it takes no iterations and simply a single pass through the image. The resultant binary image may have single "on" pixels surrounded by "off" pixels or vice versa, which is a

disadvantage of this approach. This occurs because the method only analyses the intensity of a pixel, not its surroundings. Usually, morphological procedures or connected components removal is required to complete the binary image.

3.2.2 Clustering

These algorithms divide pixels into groups (clusters) depending on one or more features in the image, such as color, intensity, texture, or image position. The clusters are not planned; instead, they depend on the image's data. Machine learning methods, such as K-means or Expectation Maximization (EM), divide the data into clusters. These iterative processes assign each pixel to the cluster with the most comparable attributes. Following the labeling of all pixels, the representative characteristics of each cluster are changed depending on the previous assignment. This step is continued until the labeling of none of the pixels changes. This approach benefits segmenting images into more than two areas in about the same amount of time.

Another benefit is that the properties of each cluster are learned and altered by the algorithm during the segmentation process rather than being predefined. A negative aspect is that the generated clusters aren't always continuous (as with thresholding). Furthermore, the approach might produce poor results if the number of clusters is incorrect. Zhang [21] developed and implemented a variation of the EM method for segmenting tissue types in MR human brain images.

3.2.3 Region growing

This class of algorithms is based on the notion of iteratively expanding one or more preset sections of the picture called seeds. Neighboring pixels are allocated to an area based on a homogeneity criterion. Their grey level is less than a threshold distance from the mean intensity of all pixels in the region. The homogeneity criterion and seed starts are the key differences between region growth algorithms. Changes in the initial seed position significantly impact the convergence time and result of these approaches [21]. The benefit of these approaches is that they link all pixels that belong to the same group. The runtime unpredictability and sensitivity to beginning circumstances are also disadvantages.

3.2.4 Edge-based methods

An edge is a line that separates two sections with different grey levels. Due to the strong relationship between region borders and boundaries, edge detection methods may be utilized as a foundation for segmentation. Most edge detection algorithms use a local derivative operator to identify sudden intensity changes. For filtering out weak edges and noise, the derivative picture is thresholded. Typically, this results in boundary pieces that must be traced and linked to a closed object contour. Edge-based algorithms can detect the outline of several objects, but they require a high level of contrast between the items and the backdrop. Filtering the gradient image for noise reduction also makes it challenging to recognize little things. Solomon *et al.* [22] applied edge detection within a user-defined area of interest for PN tumor segmentation.

3.2.5 Deformable models

Deformable models work by iteratively deforming an initial curve until it tracks the boundary of an item. The image is regarded as a potential energy field with minima at borders between objects in Kass *et al.* [23] method, called the Snakes technique. The starting curve is developed towards the lowest potential of a cost function with two components: the first is the internal forces specified by the model limitations that maintain the curve continuous and smooth.

The external pressures determined by the placement of the curve on the image (the energy potential, which is dependent on intensity, gradients, and edges) are the second component of the energy cost function. For this strategy to provide satisfactory results, the beginning curve must be positioned quite near to the item of interest in most circumstances. Another drawback of this approach is that it is challenging to trace concavities, making it inappropriate to segment tumors with complicated forms [21]. The developing contour (or surface) is represented using a signed function (the speed function) whose zero level should match the real shape in the Level Set approach. The speed of each point on the curve causes it to move inwards or outwards.

Cai *et al.* [24] utilized the level set approach to segment 3D plexiform neurofibroma tumors. After the algorithm has converged, the resultant curve continuously tracks the object's contour, even when portions of the image's boundaries are hazy or noisy, which is a significant benefit of these approaches.

3.2.6 Graph partitioning

The image is modeled as a weighted, undirected graph in these methods. Each pixel is represented as a node connected to its neighbors by edges. Edge weights represent the similarity between neighboring pixels. A graph cut divides nodes into two distinct sets, and the cut's weight is equal to the total of the weights of all edges connecting nodes from both groups. Finding the minor amount is a well-known computational issue with simple solutions. By forcing a group of pixels known to be within the item to be one side of the cut and another group known to be in the background to be the other, an object of interest may be segmented.

The minimum cut is made between pixels with the slightest similarity, frequently around the object of interest's boundary [25]. The real benefit of graph cut-based approaches is that they consider the entire picture while cutting results in globally optimum segmentation. However, the approach favors convex forms because more minor cuts are less expensive. Shape information may be incorporated into the edge weights to solve this problem. For example, Freiman *et al.* [26] used information about tubular forms in the weight function to segment blood arteries using graph cuts.

3.2.7 Prior knowledge

Most of the segmentation methods outlined above can utilize prior information about the structures of interest to decrease runtime and enhance outcomes. Prior knowledge covers intensity range, shape, size, and closeness. Prior knowledge of the tumor intensity range, for example, can help in the automatic selection of a threshold that differentiates lesions from their background, or a kidney-shaped starting model can speed kidney segmentation using deformable models. The main method for medical segmentation is prior information in an atlas (a statistical anatomical model generated from samples of healthy or ill people). Prastawa *et al.* [27] employed a probabilistic spatial atlas for brain tumor segmentation that combines prior expert information about brain structures and subject-specific priors.

3.3 MRI segmentation methods for PNs

The task of segmenting PN tumors is quite difficult. The lesions might be significant or minor, and their shapes can be complicated and irregular. They also arise in many places of the body,

infiltrating surrounding tissue and displacing organs in some cases. All previous studies rely on STIR sequence MR images because detecting lesions is much easier since they look brighter in this kind of image. But the critical point of our method is to recognize PN lesions in all MRI sequences, including STIR, T1, and T2 weighted images. The performance of my technique in the submitted manuscript (Chapter 5).

So far, only a few published studies (*e.g.*, [22], [28]–[30]) have proposed segmentation algorithms specific to this type of tumor. Most of these procedures are semi-automated, with the first tumor localization requiring user intervention. Other recent studies (e.g., [4], [31]) mainly employed these four key methods. These methods are discussed in the following sub-sections.

3.3.1 Method 1: Solomon *et al.* (2004)

Solomon *et al.* [22] presented an automated detection and volume measurement of PN using MRI in 2004. The following steps describe their segmentation algorithm:

1. Trace the lesion and include hypointense normal tissue in the ROI, omitting associated iso-intense normal tissue (this step is performed manually).

2. Use a Gaussian kernel to smooth the image.

3. Analyze pixel histograms to calculate a threshold value.

4. Remove all normal tissue from the ROI.

5. Create an image gradient to allow edge recognition.

6. Apply the thresholding value to the gradient image.

7. Remove connected components that are smaller than a predefined size.

8. Use automatic edge detection to construct the image contour.

Note that the above procedures are performed for each slice of the sequence when the ROI includes lesion tissue.

The histogram analysis from step 3 is the key novelty of the algorithm. In this step, a threshold value is selected to differentiate pixels, including normal tissues or lesions. Two histogram points

are determined automatically: Normal tissue is represented by the peak in the histogram, while the PN lesion is represented by the local maximum exceeding a predefined percentage of normal tissue peak and located to the right of this maxima (toward lower image intensities). The threshold value that separates the two tissue types is the minimum value between these peaks in the histogram. When using this type of operation, the user must include normal tissue in the initial ROI.

Although this technique removes small lesions of a predefined size (step 7), the original ROI can comprise more than one lesion. This procedure is necessary to remove noise before connecting edge components, but it comes at a cost: the inability to identify small lesions. According to the article, this is not a significant disadvantage because small lesions have a modest volume and contribute little to the overall tumor burden estimate.

In the manuscript presented in Chapter 5, I compare the method I developed with a similar version of Solomon *et al.* [22]. I was not able to replicate this method since important details were not fully described (*i.e.*, predefined size for small lesion removal and predefined percentage of normal tissue for lesion peak identification).

3.3.2 Method 2: Cai *et al.* (2009)

In 2009, Cai *et al.* [24] presented a method to identify tumors from whole-body MRI images. They studied tumor burden in patients with Neurofibromatosis types 1 and 2 and Schwannomatosis. For 3D nerve sheath tumor segmentation in MR images, a technique termed the Dynamic Threshold (DT) level set method was described. A seed area is manually initialized within the tumor as a first step. A propagating shell consisting of an inner shell, outer shell, and medial axis expands in 3D inside the slice and into subsequent slices. The volume inside the segmentation is referred to as the inner shell. The outer shell is the equal volume region that surrounds the inner shell. The medial axis divides the inner and outer shells, defining the outer shell boundaries.

A propagating shell medial axis is dynamic. Its movement is regulated by the DT speed function, which is determined for each point on the medial axis by the histogram of all voxels (pixels in 3D) in the propagating shell. When this function is positive, it pushes the points on the medial axis outward; when it is negative, it pushes them inward. The speed function is used to create the

difference between a dynamic threshold value produced from the histogram for that iteration and the intensity of a point on the medial axis. The shell is pushed closer to the tumor edge until it has an equal amount of background and tumor voxels. In the histogram, the propagating shell tumor-to-background voxel ratio is calculated by looking at a separation intensity threshold, a minimum intensity between two peaks dividing two tissue types. The threshold satisfying this condition is utilized to assess if the number of voxels reflecting the lesion and normal tissue is balanced. When the number of tumor and background voxels is balanced, or when volume changes become insignificant, the process stops.

3.3.3 Method 3: Weizman *et al.* (2012)

Weizman *et al.* [29] published a method and preliminary performance evaluation of an interactive segmentation of plexiform neurofibroma tissue in 2012. Their algorithm has two phases: a learning phase and an interaction phase. The training set is studied and learned to construct the model histogram pool during the first phase, which is performed offline and only once. A radiologist conducts the interactive phase and is blind to segment PN lesions from an MRI image reviewed for the first time. A designated region on top of an MRI slice serves as the interactive phase input. The most comparable histogram from the model histogram pool developed during the learning phase is matched to the histogram of the indicated region. The matched histogram threshold value is transformed into an actual intensity value for the current slice.

Tumors are defined as brighter pixels with intensity above the threshold and belonging to a linked component that interacts with the user input. The interactive step is repeated until the user is confident that all tumor voxels have been tagged.

The step of their algorithm is as follow:

- Offline learning phase:

  1. Preprocessing of the training set

  2. Histogram set creation

- Interactive phase of model-user driven

1. Annotation by the user

2. Histograms matching

3. The selection of the threshold

4. Removal of irrelevant connected components

The disadvantage of this method is similar to a previous tool [22] and is related to the manual adjustment step, which removes small lesions. The final calculated volume of the lesion is not very accurate since tiny lesions were removed at that step.

3.3.4 Method 4: Weizman *et al.* (2014)

In 2014, Weizman *et al.* developed another method named PNist, described as an interactive volumetric measurement of plexiform neurofibromas in MRI scans. Their approach consists of training and interaction phases as in their previous study [29]. The training phase input is a set of STIR images. These scans generate models of predicted intensity distributions, which are then saved in a histogram database. The interactive part of the method uses information from the database and the user interaction to identify PNs in the new STIR scans. The user must draw a scribble across the tumor location to give seed for the segmentation procedure during the interactive phase. Every tumor component in each image slice is fitted with two axis-aligned frames: a larger frame as the tumor region's bounding box and a tiny frame with sides half the size of the large frame situated in its center. The small frame contains most tumor pixels, whereas the big frame contains both tumor and normal surrounding tissue samples. The gray-level intensities of tumor and normal areas are modeled using these frames. The user must draw a scribble over the tumor location to give seed for the segmentation process during the interactive segmentation phase. They employ large and small frames during training to imitate two typical scribble sketching conditions. The tiny frame histogram represents situations where the user's scribble is within the tumor region and contains no healthy tissues. The big frame histogram is used to mimic instances in which the user's scrawl incorporates healthy areas in addition to cancerous pixels. These two histogram patterns are adequate to cover most scribble sketching

cases. Add advantages and cons of the method: computation time, accuracy, performance with respect to their previous method, and performance with complex disconnected lesions.

3.4 Summary

All four approaches for PN segmentation were used with MRI STIR images that perform the tumor and lesions better than other image sequences like T1 and T2. All described methods above, except Cai *et al.,* are time-consuming and laborious for the user since including two manual steps in their algorithm. The first is the ROI selection on each slice, and the second is the manual adjustment to remove the connected parts to the lesion, which affects the volume calculation of the lesion. Furthermore, Cai *et al.*'s method needs less effort: planting a seed into each tumor. It then works in three dimensions to segment the whole tumor across all slices. The problem emerges when a bright, healthy tissue is attached to the tumor, causing it to be labeled a tumor. This approach is much more computationally expensive than 2D segmentation; segmenting a single tumor might take several minutes, depending on its size and seed location. Finally, this technique necessitates more user input when many discontinuous tumor masses are involved. Because of this, they decided not to consider small lesions smaller than 5cm^3.

Our objective was to develop a fast and accurate method that reduces the manual steps and can be used with fewer limitations, such as dependency on image sequences. Unlike the earlier methods discussed above, the structural MRI input sequence does not affect our technique. It enables precise volumetric evaluation for short TI inversion recovery (STIR), T2-weighted, and T1-weighted imaging data (with or without gadolinium). Our method is unaffected by the direction (sagittal, axial, or coronal) of the original region of interest (ROI).

Chapter 4 – Introduction to the methodology

This chapter presents a short introduction of the algorithm that I implemented and described in the following chapter.

Since PNs have complex shapes, tracing lesion changes during medical treatment is challenging but essential to adjust therapy over time. The current practice to monitor changes in lesions is described in the RECIST guidelines, which consider only 1D or 2D measurements (see illustrations in Figure 7) by measuring the longest lengths of the tumor with a ruler [18]. This methodology is limited as PNs have complex and irregular shapes. Previous studies using RECIST criteria showed poor reproducibility in measuring response for similar tumors [24], [32].
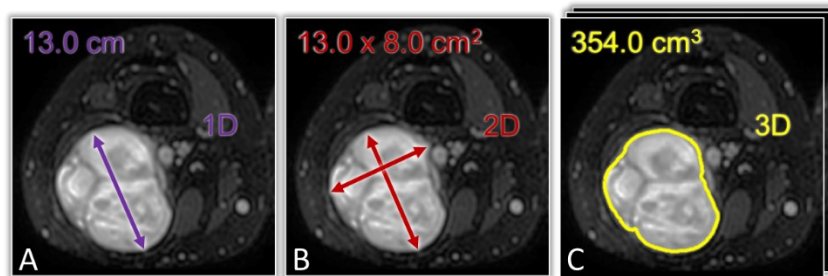
Figure 7. Comparison of three measurement approaches estimating a tumor size [19]. A, 1D measurement. B, 2D measurement. C, Volumetric analysis (3D measurement).

Previous studies have proposed volumetric analysis of PN tumors [22], [24], [28]–[30]. These studies were developed for STIR images only and limited to axial and/or coronal views. One of the essential advantages of the method developed in this study is that it can be used for different MRI sequences (STIR, T1- and T2-weighted imaging) and performs for all three orientations. Our method was compared to manual tracing, which is considered the current gold standard.

The complete methodology is provided in the submitted manuscript and replicated in the next Chapter.

4.1 Implementation

Figure 8 shows a schematic of the tool I developed for this project implemented in MATLAB (2020, version 9.9.0, Natick, MA) environment based on this study. Before employing this tool, I first require converting DICOM files (raw data from an MRI device, including the image and extensive information on the accusation) to PNG images (only gray-scale images as a 2D matrix). A short description of steps for using this tool is as follows (for reference, see Figure 8):

(1) Using the _Open_ button, input slices as PNG images. They are shown in the _List of images_ section at the left.

(2) Click on the _Draw ROI_ button. Draw a blue circle over a sub-lesion as ROI. Note that:

> - For a hollow lesion containing a hole, uncheck the _No hole in ROI_ and then click on _Draw ROI_. In this case, the hole inside will be omitted from the lesion.

> - Avoid very extensive circles with respect to the lesion size also; otherwise, the result is not logical. Our method is sensitive to the histogram analysis, so when a too big circle is selected, it often contains a less lesion area, which is bright, and a dominant dark area that can alter the histogram analysis pattern drastically.

(3) Automatically, the biggest identified lesion in ROI is shaded with green, and the _Histogram_ chart and selected _Threshold_ are shown in the bottom-right corner. You can redo the circling at this stage by clicking on _Draw ROI_ as many as you want. It is possible to manually change the threshold by scrolling the threshold gauge (at the bottom-left) between zero and one, although it is unnecessary.

(5) If the green mask matches your intention as the sub-lesion, click on the _Mask Out_ button. Here, a binary mask of that lesion is created and presented in the up-right corner (_Current Mask_). The ROI turns magenta (for future reference), and the green area is wiped. In case of multiple lesions, you must segment each at a time. New binary masks will merge with the previous.

(5) When segmentation is finished for the current slice, click the _Save Mask & Move Image_ button. This saves the _Current Mask_ in the up-right corner and moves the original segmented PNG to

another directory. Select another image from the _List of images_ and start segmenting the next slice.

For volumetric analysis, another program is required to interpolate all the masks (processed) in one orientation, providing you with the volume of the lesions and the 3D representation of the segmented tumor.
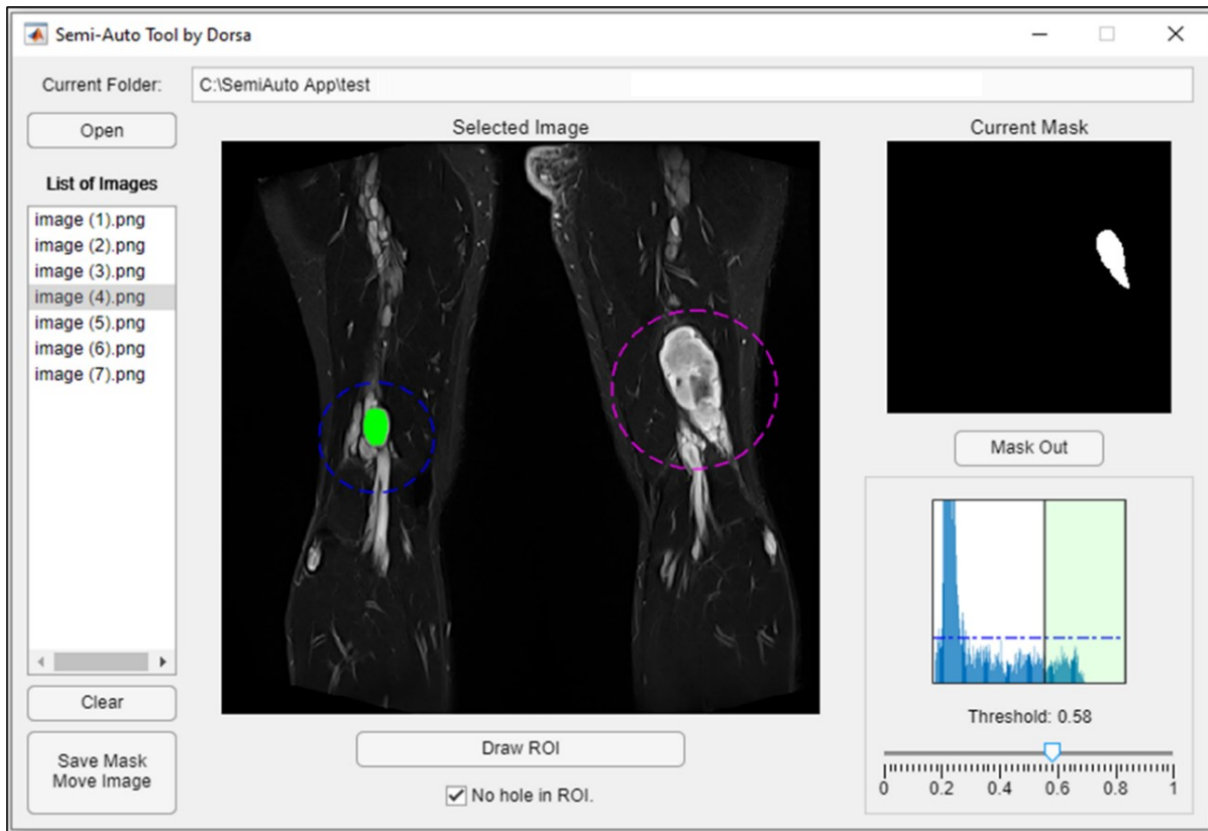
Figure 8. A scheme of the developed tool that we used for this study.

Chapter 5 – Development of a semi-automatic segmentation technique based on mean magnetic resonance imaging intensity thresholding for volumetric quantification of plexiform neurofibromas

This chapter consists of a replica of the manuscript that was submitted to the American Journal of Neuroradiology on August 18th, 2022. The manuscript details the method developed for the volumetric analysis of patients with PNs treated with trametinib. For this article, I contributed to the development of the method, data analysis, data interpretation, manuscript redaction, revision, and approval.

Dorsa Sadat Kiaei,[a,b] Jean-Claude Decarie,[c] Sébastien Perreault,[b,d,*] and Mathieu Dehaes[a,b,c,*]

[a] Institute of Biomedical Engineering, University of Montréal, Montréal, Canada

[b] Research Center, CHU Sainte-Justine Hospital University Centre, Montréal, Canada

[c] Department of Radiology, Radio-oncology and Nuclear Medicine, University of Montreal, Montreal, Canada

[d] Department of Neurosciences, University of Montreal, Montreal, Canada

[*] Equal contribution as co-senior author.

Corresponding author: Mathieu Dehaes, Ph.D. Research Centre, Sainte-Justine Hospital University Centre and the University of Montreal, 3175 Cote Sainte-Catherine, Montreal, QC, H3T1C5. Office Tel: +1 514 345 4931 #5137. Email: mathieu.dehaes@umontreal.ca

5.1 Structured Abstract

BACKGROUND AND PURPOSE: Plexiform neurofibromas (PNs) are peripheral nerve tumors that occur in 25-50% of patients with neurofibromatosis type 1. Because PNs may have complex, diffused, and irregular shapes, current clinical unidimensional measurement using magnetic resonance imaging (MRI) is limited, and volumetric assessment may prove more accurate.

MATERIALS AND METHODS: A semi-automatic segmentation technique based on *mean* image intensity thresholding (SSTMean) was developed and compared to a semi-automatic segmentation technique based on *minimum* image intensity thresholding (SSTMini). The performance (volume and computation time) of the two techniques was compared to manual tracings of 10 tumors of different locations, shapes, and sizes. Performance was also assessed using different MRI sequences.

RESULTS: When compared to manual tracing, volume quantification performed with SSTMean was not significantly different (mean difference of 2.2%), while volumes computed by SSTMini were significantly different (p <.001, mean difference of 8.2%). Volumes quantified by SSTMean were also significantly different than the ones assessed by SSTMini (p <.001). Using SSTMean, volumes quantified with short TI inversion recovery (STIR), T1-, and T2-weighted imaging were not significantly different. Computation times used by SSTMean and SSTMini were significantly different than for manual segmentation (p <.001).

CONCLUSION: Our method showed accuracy compared to a current gold standard (manual tracing). The versatility and fast computation times of our method will be useful to monitor better volumetric changes in lesions of patients enrolled in clinical trials assessing the response to therapy.

5.2 Introduction

Neurofibromatosis type 1 (NF1) is an autosomal-dominant disease that affects 1 in 3000 to 4000 individuals worldwide [33], [34]. NF1 is associated with a wide variety of physical, psychological, and cognitive manifestations. Among physical manifestations of NF1, plexiform neurofibromas (PNs) are peripheral nerve tumors that occur in 25-50% of patients [35], [36].

Plexiform neurofibromas are particularly pathognomonic for NF1 with diffuse involvement along a nerve segment and its branches. PNs affect several areas of the body (*e.g.*, head, neck, and trunk) and can cause deformity, limit function, and may lead to significant compression of vital organs depending on the size and location of the tumor [17], [29], [37], [38].

Due to the various comorbidities associated with these slowly progressing lesions, several clinical trials have been initiated over the last decade. Recent studies focused on evaluating the response to treatment with targeted therapy, including MEK inhibitors [8], [16], [39].

Response assessment of PNs is typically evaluated with magnetic resonance imaging (MRI) [29]. Tumor measurements follow uniform guidelines that allow the assessment of changes in the tumor at specific time points. Currently, the RECIST criteria are used to assess solid tumor response in most clinical trials [40], [41]. The RECIST assessment is based on the characterization of anatomical changes in tumors in one dimension. This is an important limitation for PNs as these tumors have complex and irregular shapes. Previous studies using RECIST criteria showed poor reproducibility in measuring response for similar tumors [24], [32].

Volumetric methods to assess changes in tumors from MRI data are emerging [22], [24], [29] and have been implemented in commercial platforms [4]. When compared to unidimensional assessment, volumetric approaches allow the detection of early changes in tumors and the possibility of evaluating asymmetric growth [32]. These techniques are semi-automatic and require user interaction to initially localize the tumor in the body. For several tumors, these approaches necessitated high computation times related to the segmentation process and sometimes manual corrections when the semi-automatic segmentation failed [29], [30]. A fast, reproducible, and accurate technique to assess complex and asymmetric tumor evolution is critical for clinical decision-making in clinical trials involving therapeutical assessment.

In this study, we described a semi-automatic segmentation technique based on *mean* image intensity thresholding (defined as SSTMean) that requires minimal user interaction initially to define the tumor region and that further automatically segments PN lesions. We compared SSTMean with a semi-automatic segmentation technique based on *minimum* image intensity thresholding (defined as SSTMini) that is similar to a previous approach [29]. We also compared

the performance of the two techniques with manual tracings of 10 tumors of different locations, shapes, and sizes. In contrast to previous algorithms [4], [22], [24], [29]–[31], our method is independent of the structural MRI input sequence and provides accurate volumetric assessment for short TI inversion recovery (STIR), T2-weighted, and T1-weighted (with or without gadolinium) imaging data. Our technique is also independent of the orientation (sagittal, axial, or coronal) in which the initial region-of-interest (ROI) is traced.

5.3 Material and Methods

5.3.1 Patients

Ten (N=10) patients diagnosed with PNs were selected to assess the performance of the SSTMean and SSTMini methods. These patients were enrolled as part of an ongoing clinical trial with trametinib (NCT03363217).[42] For this study, patients were selected based on the shape, location, and size of their tumors to represent a heterogeneous set of lesions. Supplementary Fig 1 shows each tumor in the three orientations using either T1, T2, and/or STIR images (except for Patient 6, who had no MRI images in the sagittal plane).

5.3.2 Data Acquisition

Based on the clinical MRI protocol, images of PNs were acquired with STIR, T1- and T2-weighted imaging sequences. Imaging parameters depended on the location, shape, and size of the tumor and were not identical for all patients (ranges are provided). Imaging parameters for STIR were repetition time (TR, ms) = [2681-5716], echo time (TE, ms) = [23-65], and inversion time (TI, ms) = [120-170], and slice number = [18-59]. For T1-weighted imaging, TR = [5-3000] ms, and TE = [1-107] ms, and [20-63] slices. For T2-weighted imaging, TR = [1328-5880] ms, TE = [60-221] ms, and [34-67] slices. Depending on the location of the tumor and the sequence, images were prescribed in either the sagittal, coronal, and/or axial orientation.

5.3.3 Segmentation Technique

The SSTMean method consisted of 4 main steps: (1) selection of the ROI, (2) smoothing of the lesion boundaries, (3) automatic calculation of the intensity threshold, and (4) generation of the lesion mask.

(1) Selection of the ROI: This process is initiated by loading MRI image files (in PNG format) and selecting the sequence of interest (STIR, T1- or T2-weighted) and the orientation (axial, coronal, or sagittal). In some cases, images acquired are not available in all orientations (*e.g.*, Patient 6 from Supplementary Fig 1). For each slice, a circle was drawn by the operator using a drawing tool to trace a circular ROI around the lesion (see an example in Supplementary Fig 2). This tracing allowed the algorithm to exclude healthy tissue surrounding the tumor. For images with no tumoral tissue, the operator did not have to draw an ROI and was guided to the next slice. The tool also allowed the operator to trace multiple ROIs when tumors appeared in multiple locations on the same slice.

(2) Smoothing of the lesion boundaries: In the ROI, a filtering method was applied to detect the edges (boundaries) of the lesion. A Gaussian smoothing filter with standard deviation σ =.5 was used and applied in both the horizontal and vertical directions to reduce the noise level of the image and allow edge detection [43].

(3) Automatic calculation of the intensity threshold: A histogram of the ROI signal intensity was performed to delineate pixels corresponding to the tumor and pixels associated with other tissues (see an example in Supplementary Fig 2). On STIR, T1- and T2-weighted images, pixels corresponding to the tumor are hyperintense while healthy tissues are hypointense. The algorithm performed the following steps to determine the image intensity threshold that differentiated healthy and tumoral tissues: 1) plot the ROI signal intensity histogram using 256 intensity bins, 2) calculate the mean of the overall distribution, 3) divide the mean by two, 4) ensure that this value is located between the two local maxima of the image (associated with healthy and tumoral tissues, respectively), and 5) assign this value as the image intensity threshold for this slice and ROI (*e.g.*, see the red threshold in Supplementary Fig 2A and its corresponding segmentation in Supplementary Fig 2B).

(4) Generation of the lesion mask: A binary mask was generated with pixels corresponding to values above the threshold. This step also allowed the generation of a mask that included multiple tumors. For granular tumors, the mask may include healthy tissues distributed and diffused between the tumoral aggregate. To be included in the mask, the operator traced an individual

ROI for each tumoral element. For multiple ROIs, individual masks were subsequently merged to yield a global binary mask.

To segment the tumors with the SSTMini method, we modified the image intensity threshold defined in step 3 by the local minimum located between the two maxima of the image (see magenta threshold in Supplementary Fig 2A and corresponding segmentation in Supplementary Fig 2D). This thresholding method was similar to a previous approach [22], [29]. The other steps were identical to SSTMean.

5.3.4 Volumetric Quantification

To determine the tumor volume, the boundaries of two consecutive slices were linearly interpolated, and the tumor was reconstructed in a 3D shape. This reconstruction was based on the slice spacing, slice thickness, and spatial resolution in the slice plane. Total volume corresponded to the sum of all merged slices.

5.3.5 Manual Tumor Tracing

There is no gold standard for the volumetric quantification of PNs. Tumor volumes generated by SSTMean and SSTMini methods were then compared with the manual tracing of the tumors (*e.g.*, Supplementary Fig 2E).

5.3.6 Statistical Analysis

Wilcoxon signed-rank tests were used to compare the volumetric quantification of the tumors performed by the three techniques: SSTMean, SSTMini, and manual tracing. Differences between techniques were expressed in percentage in comparison to manual tracing. Computations times were also compared between the three techniques using Wilcoxon signed-rank tests.

5.4 Results

Figure 9 shows 4 examples (Patient 4, 5, 6, and 10) of lesion segmentation performed by SSTMean (red) and SSTMini (magenta) in comparison with manual tracing (yellow). MRI STIR images were used for these examples.

Table 1 reports tumor volumes quantified by SSTMean, SSTMini, and manual tracing for all patients, as well as computation times. Volume percentage differences between SSTMean and SSTMini with manual tracing are also provided. For each patient, volume quantification was performed using the three sequences (STIR, T1- and T2-weighted images). When compared to manual tracing, volume quantification performed with SSTMean was not significantly different (p=.38), while volumes computed by SSTMini were significantly different (p <.001). Volumes quantified by SSTMean were also significantly different than the ones assessed by SSTMini (p <.001). Using SSTMean, volumes quantified with the STIR, T1- and T2-weighted imaging sequences were not significantly different. Differences between MRI orientations were not assessed since orientations were prescribed based on the location of the tumor. Computation times used by SSTMean and SSTMini were significantly different from computation times used by manual tracing (p <.001).
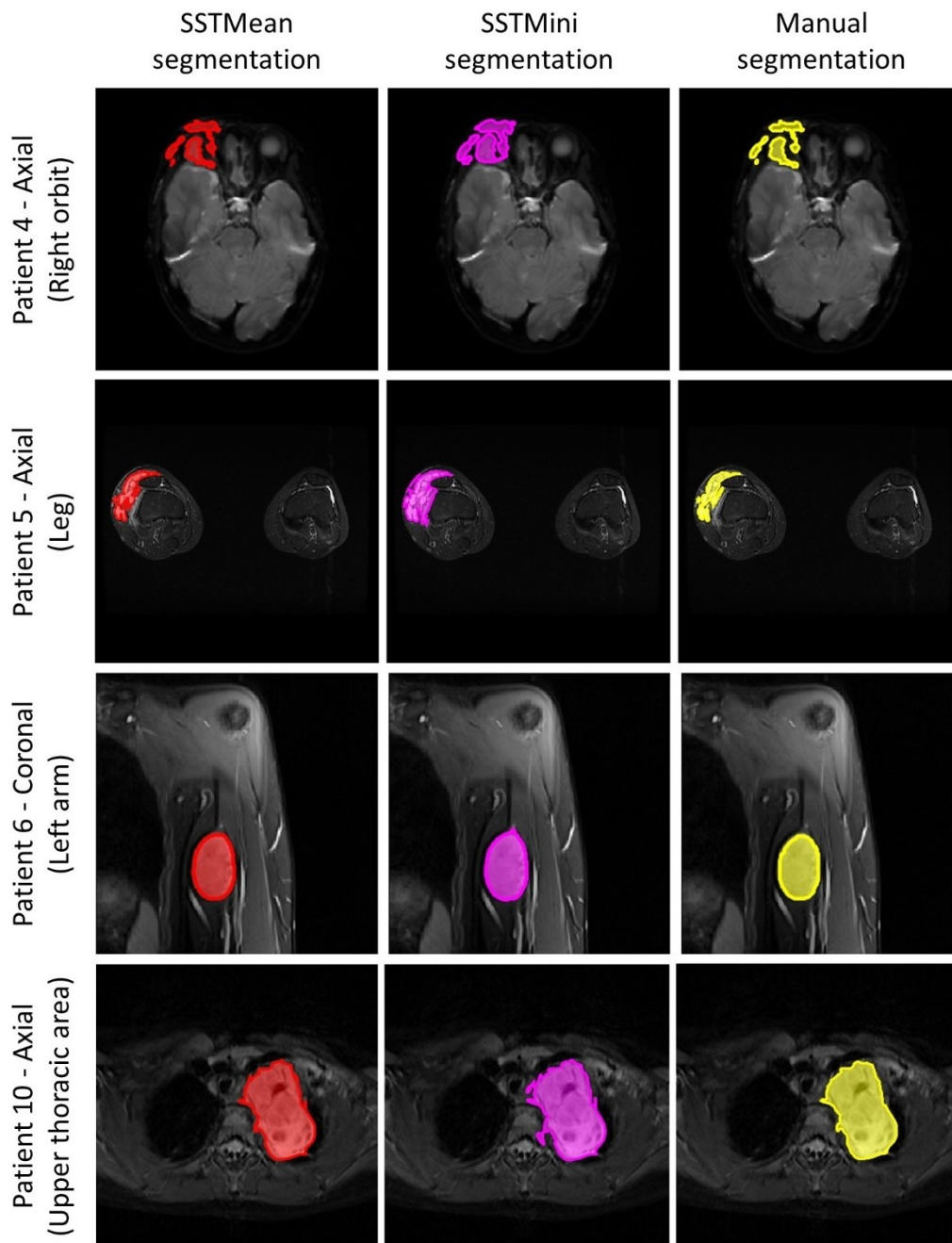
Figure 9. Examples (Patient 4, 5, 6, and 10) of lesion segmentation performed by SSTMean (red), SSTMini (magenta), and manual tracing (yellow) for a single 2D STIR image.

5.5 Discussion

The goal of this study was to develop a fast, reproducible, and accurate method to quantify the volume of PNs in the setting of a clinical trial. The proposed segmentation method required only

one minimal user interaction for each MRI slice, which resulted in faster computation time (4-10 min) compared to manual tracing (23-59 min) of the total lesion. Lesion volumes quantified by the SSTMean method were not statistically different from that of manual segmentation (gold standard), which shows its accuracy. The performance of our method was accurate for a wide range of lesion sizes, from small (~3 cm^3) to large (~375 cm^3) lesions. Our method was also versatile and reproducible, providing accurate volumes regardless of the MRI sequence (STIR, T1- or T2-weighted imaging) and view (axial, coronal, or sagittal).

The technique developed in this study was compared to another algorithm (SSTMini) that we implemented, similar to a previous approach [22]. Compared to the SSTMini method, our algorithm provided more accurate volumes with respect to manual quantification (mean difference of 2.2% compared to 8.2%). The thresholding aspect of our method may be useful to monitor better volumetric changes in lesion progression of patients enrolled in clinical trials assessing the response of therapy.

The comparison between our proposed method with SSTMini was relevant as the two techniques have in common several methodological aspects. However, it was not possible to replicate this exact published method as important details were not fully described in the original article [22]. While the two methods are based on a similar thresholding technique, the identification of the PN lesion peak in the published method was based on a predefined percentage of normal tissue that was not available. The published method also performs a connected component analysis to remove lesions that were considered too small. There is no detail on this predetermined size. Another study used a similar approach and did not consider lesions of less than 5 cm^3 [24]. Our approach was different and considered all lesions of all sizes. This strategy, coupled with a finer thresholding technique, may explain why our method was more accurate than SSTMini when compared to manual tumor quantification. The assessment of all lesions of any size may help global surveillance of a patient during treatment.

Other segmentation approaches were previously developed for solid tumors, such as PNs [22], [24], [29], [30]. Some of these algorithms were implemented on commercial visualization and analysis software such as MEDx [4], [22], [24], [28], [31], Vitrea2 workstation [31], and 3DQI

software [28], or separately programmed as PNist [29], [30]. We implemented our algorithm using the MATLAB (2020, version 9.9.0, Natick, MA) environment.

Above mentioned algorithms and ours were semi-automatic and required user involvement initially to locate the tumor in the image. However, their segmentation procedure differed. In the method described by Cai *et al.* [24], the thresholding approach is dynamic and based on a 3D level set method. After an initial user interaction to identify the tumor location, tumors larger than 5 cm^3 in diameter were automatically segmented in 3D. The method described by Weizman *et al.* [30] is interactive and based on histogram tumor models from a training set. In their process, which differs from ours and previous approaches [22], [24], the user is required to draw a scribble over the tumor region that provides seed for segmentation. A previous study [29] from the same group showed that their interactive approach was simpler and more reliable, particularly for complex, disconnected tumors, even if, for some tumors, a manual correction was inevitable. Their approach was accurate (6.8%) and fast (7 min) when compared to manual tracing [30]. This comparison with previous state-of-the-art tools shows that our method is slightly more accurate and consumes similar computational resources.

Two advantages of our method are that it (1) can be applied to different MRI sequences (STIR, T1-, and T2-weighted imaging; with or without gadolinium) and (2) performs for all three orientations (axial, coronal, and sagittal). Previous studies implemented algorithms that were used only for STIR images and were limited to axial and/or coronal views [22], [29], [30]. The versatility of our approach may prove useful in the clinical setting where MRI sequences and prescribed orientations may be limited due to imaging time constraints which can be critical, especially in children. In addition, this possibility may help to optimize imaging data based on tumor location, shape, and size. Using the multiple orientations and sequences may also help to validate volume assessment for complex tumors with irregular shapes.

Our algorithm has limitations. As in previous approaches, the need for user interaction initially to define the tumor ROI in every single slice slows volume quantification. This limitation is amplified for tumors with multiple disconnected lesions. Novel approaches such as using large datasets to train data and mathematical models to predict volume changes are promising and may allow

avoiding any user interaction [29], [30]. The accuracy of our method is also limited by artifacts and low MRI image quality, which can affect the ROI selection and subsequent thresholding calculation based on mean image intensity. Because there is no current gold standard for tumor volume quantification, the use of manual segmentation to compare our approach is intrinsically a limitation. To the best of our knowledge, manual tracing remains the most accurate standard for comparison.

The simplicity and accuracy of our method may allow its implementation in clinics to evaluate response rates in future trials. The algorithm could be integrated into the imaging platforms such as picture archiving and communication systems (PACS). This integration would avoid the need to extract, transfer, and anonymize MRI data. Volume outputs from the algorithm could be included in radiological reports in real-time and shared with the patient at the time of MRI. This algorithm has the potential to be used for various peripheral solid tumors as well as for central nervous systems tumors. Due to fast computation, volumetric analysis of response to therapy or tumor progression could be analyzed and reported at the time of patient's follow-up visits.

5.6 Conclusion

Volumetric analysis and MRI image segmentation are essential for analyzing PNs and following their progression. To quantify tumor volume, we proposed a semi-automatic segmentation technique based on mean image intensity thresholding and compared it with the current gold standard (manual tracing). Our method showed high accuracy and versatility as it did not depend on MRI sequences or orientation planes. Our method was used to quantify lesions from 3 to 375 cm^3. As in previous algorithms, our technique was fast and necessitated only one manual step associated with the ROI selection, which is promising for further clinical integration and use in clinical trials assessing the response of therapy.

5.7 Acknowledgment

Table 1: Volumetric quantification of tumors performed by SSTMean, SSTMini, and manual tracing with corresponding computation times.

Patients		SSTMean			SSTMini			Manual tracing	
		Volume (cm^3)	Comp. time (Min)	Difference[*] (%)	Volume (cm^3)	Comp. time (Min)	Difference[†] (%)	Volume (cm^3)	Comp. time (Min)
Patient 1	Sag STIR	377.1	7	0.6	411.3	7	9.7	374.8	53
	Ax T1	375.6	6	-0.5	416.2	6	10.3	377.4	50
	Cor T2	376.4	7	0.4	412.5	7	10.1	374.8	55
Patient 2	Ax STIR	8.9	7	-2.2	9.7	7	6.6	9.1	59
	Cor T1	8.8	8	-3.3	9.8	8	7.7	9.1	56
	Sag T2	8.7	5	-6.5	10.1	5	8.6	9.3	53
Patient 3	Ax STIR	37.5	6	3.0	39.2	6	7.7	36.4	43
	Sag T1	38.1	7	1.6	39.9	7	6.4	37.5	50
	Cor T2	37.3	6	3.3	38.8	6	7.5	36.1	48
Patient 4	Ax STIR	46.7	5	1.7	48.1	5	4.8	45.9	46
	Sag T1	45.8	7	2.0	46.3	7	3.1	44.9	50
	Cor T2	47.2	6	1.9	49.2	6	6.3	46.3	45
Patient 5	Ax STIR	442	8	1.1	461.8	8	5.7	437	56
	Sag T1	444	8	1.4	463.2	8	5.8	438	58
	Cor T2	437	7	1.2	458	7	6.0	432	55
Patient 6	Cor STIR	3.1	5	-8.8	4.2	5	23.5	3.4	31
	Cor T1	3	7	-3.2	4.1	7	32.3	3.1	38
	Ax T2	3.2	6	-3.0	4.6	6	39.4	3.3	36
Patient 7	Cor STIR	23.7	4	-0.4	24.1	4	1.3	23.8	28
	Sag T1	23.6	6	-0.4	24	6	1.3	23.7	31

	Ax T2	23.8	5	-5.2	24.5	5	-2.4	25.1	30
Patient 8	Ax STIR	37.7	4	2.7	39.4	4	7.4	36.7	25
	Sag T1	37.6	6	-1.1	39.1	6	2.9	38	32
	Cor T2	37.3	5	-2.1	39.2	5	2.9	38.1	30
Patient 9	Ax STIR	8.5	4	-1.2	8.8	4	2.3	8.6	23
	Cor T1	8.2	6	-2.4	9.2	6	9.5	8.4	28
	Sag T2	8.3	5	-2.4	9.1	5	7.1	8.5	25
Patient 10	Ax STIR	99.4	9	-0.8	103.2	9	3.0	100.2	57
	Sag T1	99	10	-0.4	100.6	10	1.2	99.4	59
	Cor T2	99.3	10	-0.5	101.7	10	1.9	99.8	58
Mean (SD)‡	NA	NA	6.4 (1.6)	2.2 (1.9)	NA	6.4 (1.6)	8.2 (8.7)	NA	43.6 (12.4)

Comp.: Computation; **STIR:** Short TI Inversion recovery MRI (magnetic resonance imaging) sequence; **T1:** T1-weighted MRI sequence; **T2:** T2-weighted MRI sequence; **Ax:** in axial view MRI sequence; **Cor:** in coronal view MRI sequence; **Sag:** in sagittal view MRI sequence; **Difference***: Volumetric percentage differences between SSTMean and manual tracing (gold standard); **Difference†:** Volumetric percentage differences between SSTMini and manual tracing; **Mean (SD)‡:** Mean and standard deviation of absolute percentage differences and computation times; **NA:** Not applicable.

Chapter 6 – General discussion, Preliminary data, and Prospective studies

6.1 Impacts of project

As stated in Chapter 1, a good measurement of PNs is essential to follow up on the effectiveness of the treatment. The efficiency and precision of the measures are now being improved through computer-aided techniques. Based on the performance of the method described in the manuscript, I showed the possibility of performing volumetric quantification for three different MRI sequences (*i.e.*, T1-, T2-weighted, and STIR) and all three orientations (*i.e.*, Axial, Coronal, and sagittal views).

I proposed a semi-automatic (partly manual and partly with the help of a computer) volumetric analysis approach. This method enables faster segmentation than manual tracing employing the computer for reliable 3D measurements rather than standard 1D or 2D methods (see Figure 7). Not only that, but this method was faster compared to some similar approaches and shows that our method has less difference (with respect to the gold standard) than a similar previous method.

The proposed method has the potential to become a stand-alone tool for the volume quantification analysis used for clinical purposes and join common platforms like PACS [19] to help physicians with their needs.

6.2 Preliminary data

Prior to this thesis, so far, there were 34 patients analyzed in this study out of 45 enrolled participants. MRI data was gathered from centers including CHU Sainte-Justine (CHUSJ), Montreal Children's Hospital (MCH), CHU de Québec-Université Laval (CHUQ), The Hospital for Sick Children (SickKids), IWK Health Centre (IWK), Alberta Children's Hospital (ACH), and British Columbia Children's Hospital (CWHC). Patients are between [1 month – 25 years] old.

The first date of MRI imaging was at the start of the treatment (defined as the Baseline) and then every three months (based on the scheduled MRI exam dates) until the end of the treatment, which is the 18th month.
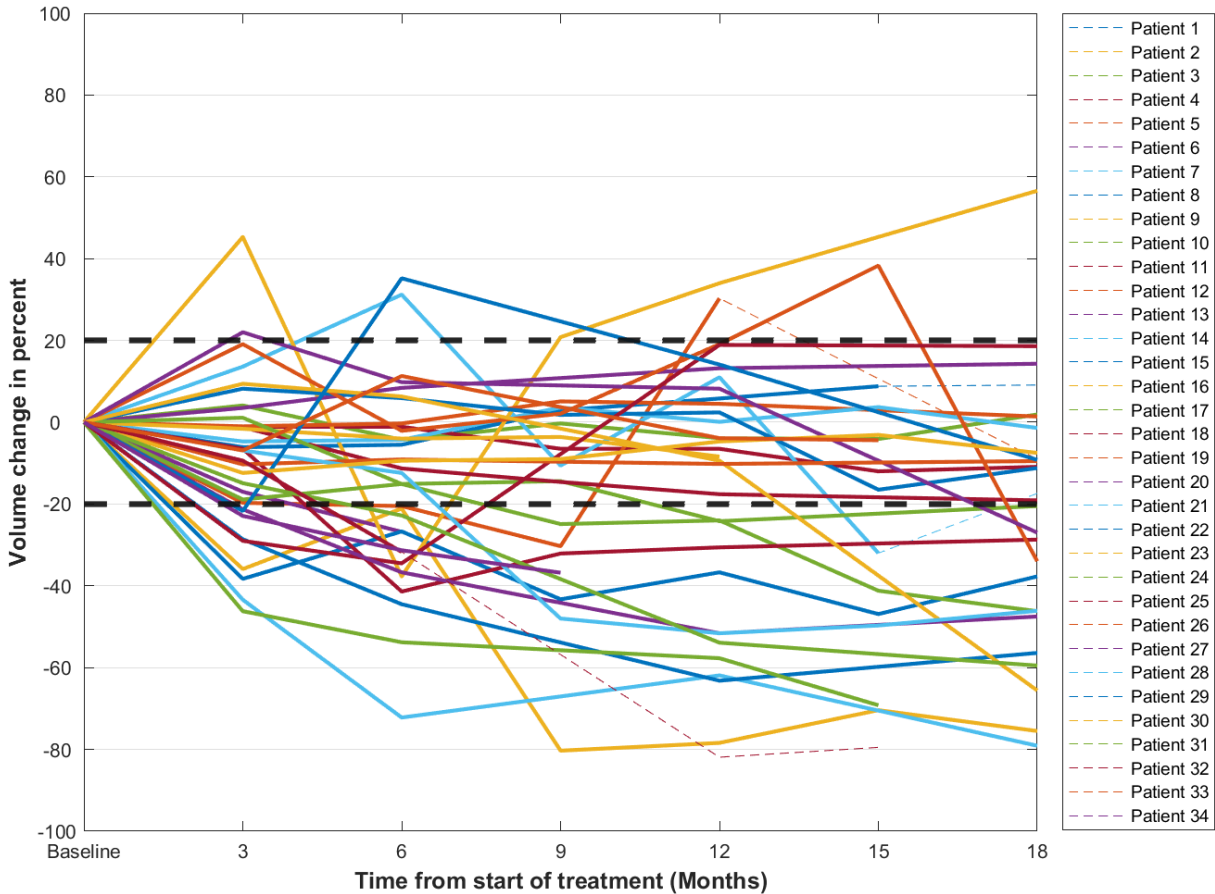

Figure 10. Combined demonstration of volume changes during the treatment cycle for all 34 patients analyzed in this study. Screening for all patients starts from the *Baseline* and is present in different colored lines. The straight, bold lines are during the treatment cycle, and the dashed lines are the follow-up dates. Two horizontal black dashed lines limit the progression and response at 20% and -20% of baseline volume, respectively.

Figure 10 represents the evolution of volumetric PN through treatment with trametinib in the study. Twenty-one patients achieved a decrease in the lesion's volumes during the treatment cycle (18 Months) by at least 20%, which means a response to the treatment.

Figure 11 shows the median variation of PN volumes over time in the treatment cycle for 34 patients and presents the -20% reduction in volumes and the effectiveness of the treatment.

These preliminary results show that our method is helpful for clinical trials since it can calculate even minor volume changes and help physicians track the volume changes during the treatment cycle.
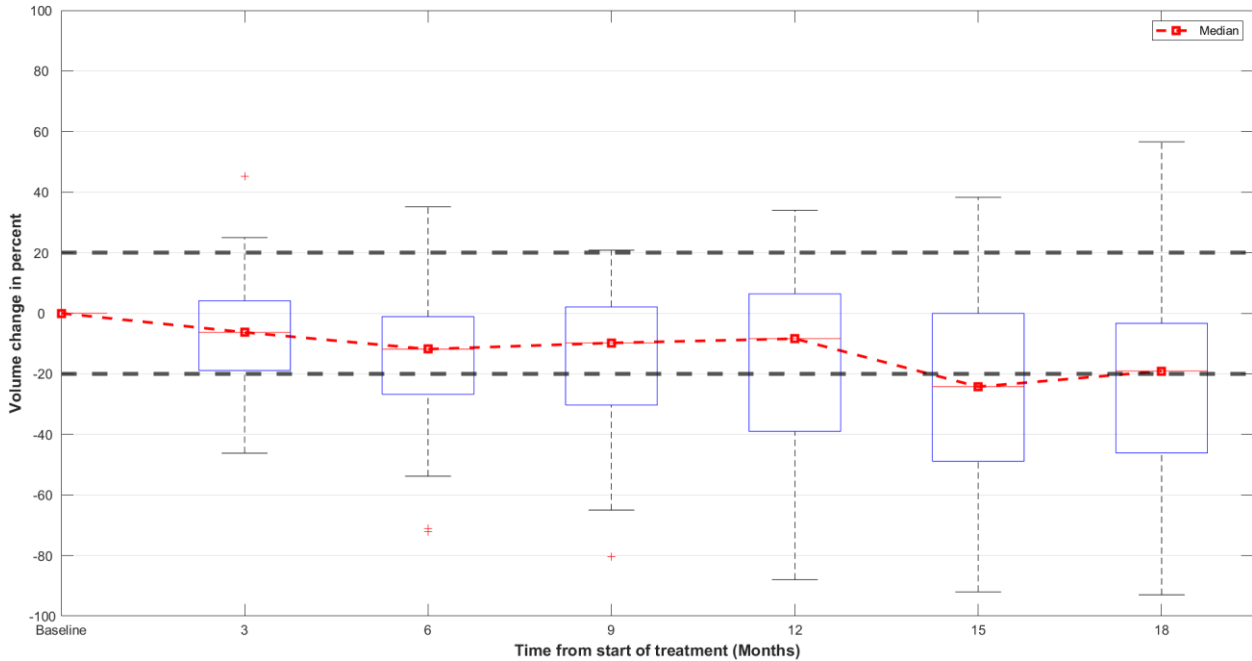

Figure 11. Median variation (with intervals-lowest and highest) of PN volumes over time (of 34 patients results in Figure 10). The median baseline volume reduces about 20% less at the end of treatments.

6.3 Limitations and potential future improvements

In the developed method, I linearly interpolate between slices to quantify the tumor volume from stacked slices. This simplification is something that should be improved, and it can be done by 3D reconstruction employing an orthogonal orientation mask, for example, using Axial and Sagittal results to create one final 3D object.

Only one user intervention for the whole process in each slice existed in the suggested method. I demonstrated that the proposed segmentation required a group of circular areas (one-by-one) centered on sub-lesions that merge, resulting in a final ROI. Instead, a previous approach [22] traced the edge of the PN lesions cluster, namely a rough region over the PN. The developed method analyses sub-lesions one at a time, eliminating the manual adjustment step at the end (the final step in [22]). Our strategy increases repetition while decreasing manual tracing (More

circles and repetitive computation). These modifications 1) improve accuracy by focusing the histogram analysis on every sub-lesion, and 2) the time for making an ROI is less labor intensive and more straightforward. Consequently, I anticipate that our approach will reduce total segmentation time in reality. Unfortunately, there is no acceptable benchmark to compare with the study's computing time [22].

As stated in Chapter 3, many other advancements exist in MRI segmentation in general. Some are useful, and some are problematic to employ for segmenting PNs. For example, a dynamic threshold recognizing normal and tumor tissue instead of SSTMean is valuable since PNs can locate everywhere in the body, and the quality of images may vary from time to time.

Also, probabilistic methods help track the lesion across slices. Thus, they can optimize the human intervention to only a few selected slices rather than all sets of MRI images.

Machine learning-assisted algorithms can help to validate real-time segmentation based on a set of pre-segmented lesions and reduce labor-intensive parts. However, this field is relatively new, and the research is ongoing.

In our proposed method, there is a lack of inter-observers analyses to show the reliability of the technique and steps that can affect from person to person.

Conclusion

For assessing PNs and tracking their evolution, volumetric analysis and MRI image segmentation are essential. We developed a semi-automatic segmentation approach based on mean image intensity thresholding to estimate tumor volume and showed its accuracy compared to the available gold standard (manual tracing). Since our technique was independent of MRI sequences or orientations, it demonstrated remarkable versatility and reproducibility. We measured lesions of a wide range of sizes (3 cm^3 to 375 cm^3). Our method, promising for future clinical integration and application in clinical trials measuring the benefits of treatment, was fast and required just one manual step related to the ROI selection for each slice.

The simplicity and accuracy of our method may allow its implementation in clinics to evaluate response rates in future studies. The algorithm could be integrated into current imaging platforms, such as picture archiving and communication systems (PACS). This integration would avoid the need to extract, transfer, and anonymize MRI data. Volume outputs from the algorithm could be included in radiological reports in real-time and shared with the patient during follow-up visits. This algorithm may be used for other types of tumors, including central nervous systems tumors.

Our algorithm has some limitations. Volume quantification is slowed down by the requirement for user interaction to determine the initial tumor ROI. This restriction is much more obvious in tumors with several unconnected lesions. Innovative methods, such as predicting volume changes by training data and mathematical models on massive datasets, are promising and may eliminate the need for human interaction [29], [30]. Artifacts and poor MRI image quality can impact the ROI selection and subsequent thresholding calculation based on mean image intensity, which further limits the accuracy of our technique. Using manual segmentation to compare our technique is inherently a drawback as there is currently no other gold standard for tumor volume measurement. To generate a 3D volume, we employ linear interpolation between slices. In a future investigation, we plan to analyze a whole-body scan in all available orientations using the segmentation approach adopted in this work. It is preferable to do manual tracing with a variety of experts (inter-observers analysis) to improve the accuracy of the gold standard.

Overall, the developed method presented in this study exhibited the ability to use for volumetric quantification of PNs. The introduced MRI segmentation method was relatively faster than manual tracing (the gold standard), reducing processing time from 44 MIN to 6 MIN on average while keeping a fair similarity to the gold standard result. The described method showed fewer variations from the gold standard volumes (2.2±1.9 %) in comparison to at least one previous method (8.2±8.7 %). The technique has the potential, and preliminary is proven to become a helpful tool for clinical purposes and help physicians to quantify PN lesions in 3D (Volume) instead of 1D and 2D measurements.

Bibliographic References

[1]   D. S. Kiaei *et al.*, "NFB-08. TRAM-01: A Phase 2 study of trametinib for pediatric patients with neurofibromatosis type 1 and plexiform neurofibromas," *Neuro-Oncology*, vol. 24, no. Supplement_1, pp. i129–i129, 2022, [Online]. Available: https://academic.oup.com/neuro-oncology/article/24/Supplement_1/i129/6601029

[2]   J. Wasa *et al.*, "MRI features in the differentiation of malignant peripheral nerve sheath tumors and neurofibromas," *American Journal of Roentgenology*, vol. 194, no. 6, pp. 1568–1574, Jun. 2010, doi: 10.2214/AJR.09.2724.

[3]   K. Staser, F. C. Yang, and D. W. Clapp, "Pathogenesis of plexiform neurofibroma: Tumor-stromal/hematopoietic interactions in tumor progression," *Annual Review of Pathology: Mechanisms of Disease*, vol. 7. pp. 469–495, 2012. doi: 10.1146/annurev-pathol-011811-132441.

[4]   E. Dombi *et al.*, "NF1 plexiform neurofibroma growth rate by volumetric MRI Relationship to age and body weight," 2007. [Online]. Available: www.neurology.org

[5]   R. J. Packer and T. Rosser, "Therapy for Plexiform Neurofibromas in children With neurofibromatosis 1: An overview," *J Child Neurol*, vol. 17, no. 8, pp. 638–641, 2002.

[6]   Y. Ji, B. Xu, X. Wang, W. Liu, and S. Chen, "Surgical treatment of giant plexiform neurofibroma associated with pectus excavatum," *Journal of Cardiothoracic Surgery*, vol. 6, no. 1, Sep. 2011, doi: 10.1186/1749-8090-6-119.

[7]   A. Banerjee *et al.*, "A phase i trial of the MEK inhibitor selumetinib (AZD6244) in pediatric patients with recurrent or refractory low-grade glioma: A Pediatric Brain Tumor Consortium (PBTC) study," *Neuro-Oncology*, vol. 19, no. 8, pp. 1135–1144, Aug. 2017, doi: 10.1093/neuonc/now282.

[8]   A. M. Gross *et al.*, "Selumetinib in children with inoperable plexiform neurofibromas," *New England Journal of Medicine*, vol. 382, no. 15, pp. 1430–1442, Apr. 2020, doi: 10.1056/nejmoa1912735.

[9]   R. Ronsley *et al.*, "Trametinib therapy for children with neurofibromatosis type 1 and life-threatening plexiform neurofibroma or treatment-refractory low-grade glioma," *Cancer Medicine*, vol. 10, no. 11, pp. 3556–3564, Jun. 2021, doi: 10.1002/cam4.3910.

[10]   C. Miller, D. Guillaume, K. Dusenbery, H. B. Clark, and C. Moertel, "Report of effective trametinib therapy in 2 children with progressive hypothalamic optic pathway pilocytic astrocytoma: Documentation of volumetric response," *Journal of Neurosurgery: Pediatrics*, vol. 19, no. 3, pp. 319–324, Mar. 2017, doi: 10.3171/2016.9.PEDS16328.

[11]   N. Manoharan *et al.*, "Trametinib for the treatment of recurrent/progressive pediatric low-grade glioma," *Journal of Neuro-Oncology*, vol. 149, no. 2, pp. 253–262, Sep. 2020, doi: 10.1007/s11060-020-03592-8.

[12]   S. Perreault *et al.*, "A phase 2 study of trametinib for patients with pediatric glioma or plexiform neurofibroma with refractory tumor and activation of the MAPK/ERK pathway," 2022.

[13]   A. Harder, "MEK inhibitors - novel targeted therapies of neurofibromatosis associated benign and malignant lesions," *Biomarker Research*, vol. 9, no. 1. BioMed Central Ltd, Dec. 01, 2021. doi: 10.1186/s40364-021-00281-0.

[14]   S. Perreault *et al.*, "A phase 2 study of trametinib for patients with pediatric glioma or plexiform neurofibroma with refractory tumor and activation of the MAPK/ERK pathway: TRAM-01," *BMC Cancer*, vol. 19, no. 1, Dec. 2019, doi: 10.1186/s12885-019-6442-2.

[15]   R. G. M. Ansorge, *The Physics and Mathematics of MRI*. 2016.

[16]   P. Therasse *et al.*, "New guidelines to evaluate the response to treatment in solid tumors," *J Natl Cancer Inst*, vol. 92, no. 3, pp. 205–216, Feb. 2000, [Online]. Available: https://academic.oup.com/jnci/article/92/3/205/2965042

[17] M. Gosein, A. Ameeral, R. Banfield, and M. Mosodeen, "Plexiform Neurofibroma of the Wrist: Imaging Features and When to Suspect Malignancy," *Case Reports in Radiology*, vol. 2013, pp. 1–4, 2013, doi: 10.1155/2013/493752.

[18] J. Oh Park *et al.*, "Measuring response in solid tumors: comparison of RECIST and WHO response criteria," *Jpn J Clin Oncol*, vol. 33, no. 10, pp. 533–537, 2003, [Online]. Available: https://academic.oup.com/jjco/article/33/10/533/883274

[19] "MRI database of CHU Sainte-Justine," 2022.

[20] D. L. Pham, C. Xu, and J. L. Prince, "Current methods in medical image segmentation 1," *Annu Rev Biomed Eng*, vol. 2, pp. 315–337, 2000, [Online]. Available: www.annualreviews.org

[21] Y. Zhang, M. Brady, and S. Smith, "Segmentation of brain MR images through a hidden Markov random field model and the expectation-maximization algorithm," *IEEE Transactions on Medical Imaging*, vol. 20, no. 1, pp. 45–57, Jan. 2001, doi: 10.1109/42.906424.

[22] J. Solomon, K. Warren, E. Dombi, N. Patronas, and B. Widemann, "Automated detection and volume measurement of plexiform neurofibromas in neurofibromatosis 1 using magnetic resonance imaging," *Computerized Medical Imaging and Graphics*, vol. 28, no. 5, pp. 257–265, Jul. 2004, doi: 10.1016/j.compmedimag.2004.03.002.

[23] M. Kass, A. Witkin, and Terzopoulos Demetri, "Snakes: Active contour models," *International Journal of Computer Vision*, vol. 1, pp. 321–331, 1988.

[24] W. Cai *et al.*, "Tumor burden in patients with neurofibromatosis types 1 and 2 and schwannomatosis: determination on whole-body MR images," *Radiology*, vol. 250, no. 3, pp. 665–675, Mar. 2009, doi: 10.1148/radiol.2503080700.

[25] J. Shi and J. Malik, "Normalized cuts and image segmentation," *TRANSACTIONS ON PATTERN ANALYSIS AND MACHINE INTELLIGENCE*, vol. 22, no. 8, pp. 888–905, 2000.

[26] M. Freiman *et al.*, "Vessels-cut: A graph based approach to patient-specific carotid arteries modeling," Berlin, Nov. 2009.

[27] M. Prastawa, E. Bullitt, N. Moon, K. van Leemput, and G. Gerig, "Automatic brain tumor segmentation by subject specific modification of atlas priors," *Academic Radiology*, vol. 10, no. 12, pp. 1341–1348, 2003, doi: 10.1016/S1076-6332(03)00506-3.

[28] W. Cai *et al.*, "Volumetric MRI analysis of plexiform neurofibromas in neurofibromatosis Type 1: Comparison of two methods," *Academic Radiology*, vol. 25, no. 2, pp. 144–152, Feb. 2018, doi: 10.1016/j.acra.2017.09.004.

[29] L. Weizman *et al.*, "Interactive segmentation of plexiform neurofibroma tissue: method and preliminary performance evaluation," *Medical and Biological Engineering and Computing*, vol. 50, no. 8, pp. 877–884, Aug. 2012, doi: 10.1007/s11517-012-0929-1.

[30] L. Weizman *et al.*, "PNist: interactive volumetric measurements of plexiform neurofibromas in MRI scans," *International Journal of Computer Assisted Radiology and Surgery*, vol. 9, no. 4, pp. 683–693, Jul. 2014, doi: 10.1007/s11548-013-0961-0.

[31] E. Dombi *et al.*, "Recommendations for imaging tumor response in neurofibromatosis clinical trials," 2013. [Online]. Available: www.neurology.org

[32] C. C. Jaffe, "Response assessment in clinical trials: Implications for sarcoma clinical trial design," *The Oncologist*, vol. 13, no. S2, pp. 14–18, Apr. 2008, doi: 10.1634/theoncologist.13-s2-14.

[33] K. Jett and J. M. Friedman, "Clinical and genetic aspects of neurofibromatosis 1," *Genetics in Medicine*, vol. 12, no. 1, pp. 1–11, Jan. 2010, doi: 10.1097/GIM.0b013e3181bf15e3.

[34] V. C. Williams, J. Lucas, M. A. Babcock, D. H. Gutmann, B. Bruce, and B. L. Maria, "Neurofibromatosis type 1 revisited," *Pediatrics*, vol. 123, no. 1. pp. 124–133, Jan. 2009. doi: 10.1542/peds.2007-3204.
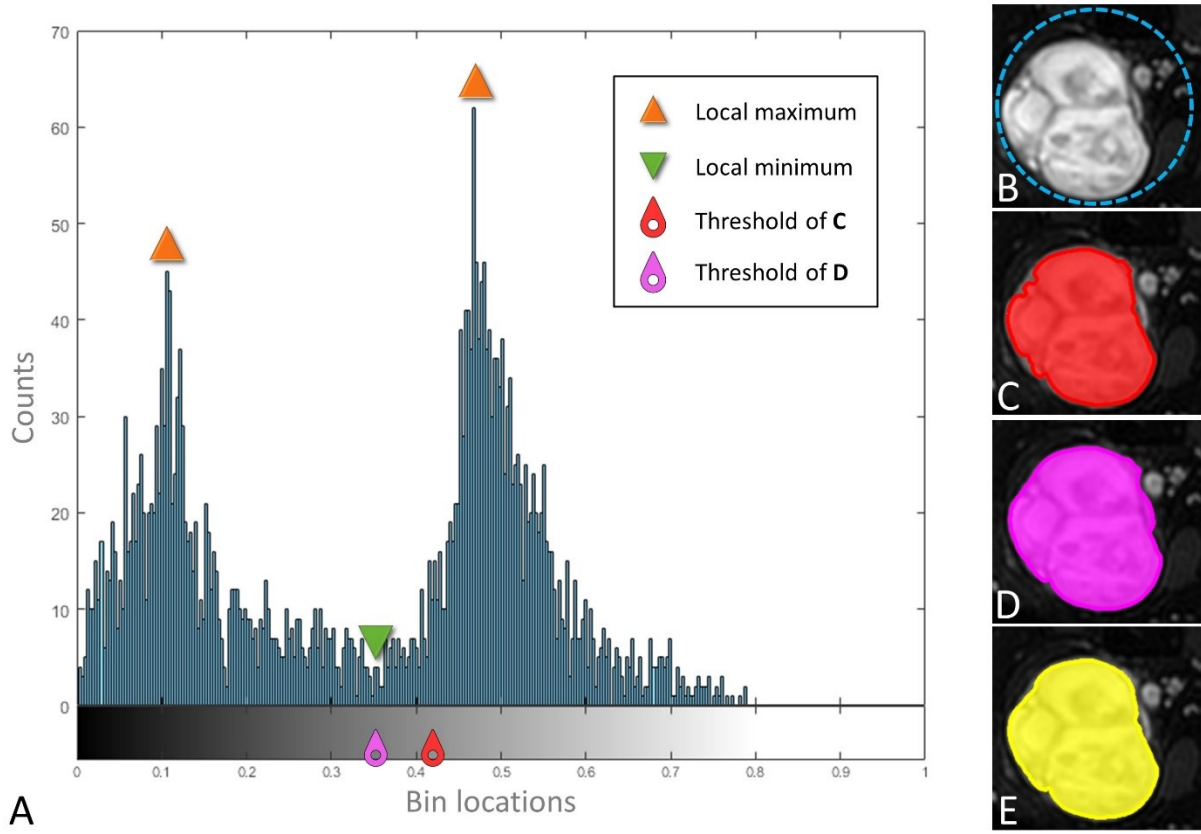
[35] A. M. Gross *et al.*, "Association of plexiform neurofibroma volume changes and development of clinical morbidities in neurofibromatosis 1," *Neuro-Oncology*, vol. 20, no. 12, pp. 1643–1651, Nov. 2018, doi: 10.1093/neuonc/noy067.

[36] K. L. Struemph *et al.*, "Adolescents and young adults with neurofibromatosis type 1: A descriptive study of adaptive functioning," *American Journal of Medical Genetics Part A*, Nov. 2021, doi: 10.1002/ajmg.a.62544.

[37] S. Akshintala *et al.*, "Longitudinal evaluation of peripheral nerve sheath tumors in neurofibromatosis type 1: growth analysis of plexiform neurofibromas and distinct nodular lesions," *Neuro-Oncology*, vol. 22, no. 9, pp. 1368–1378, Sep. 2020, doi: 10.1093/neuonc/noaa053.

[38] J. M. Boulanger and A. Larbrisseau, "Neurofibromatosis type 1 in a pediatric population: Ste-Justine's experience," *Canadian Journal of Neurological Sciences*, vol. 32, no. 2. Canadian Journal of Neurological Sciences, pp. 225–231, 2005. doi: 10.1017/S0317167100004017.

[39] A. 8 Miller, M. Staquet, A. Winkler, and A. C. C. Junqueira, "Reporting results of cancer treatment," *Cancer*, vol. 47, pp. 207–214, 1981.

[40] G. J. S. Rustin *et al.*, "Definitions for response and progression in ovarian cancer clinical trials incorporating recist 1.1 and CA 125 agreed by the gynecological cancer intergroup (GCIG)," *International Journal of Gynecological Cancer*, vol. 21, no. 2. pp. 419–423, Feb. 2011. doi: 10.1097/IGC.0b013e3182070f17.

[41] V. Semiglazov, "RECIST for response (clinical and imaging) in neoadjuvant clinical trials in operable breast cancer," *Journal of the National Cancer Institute - Monographs*, vol. 2015, no. 51, pp. 21–23, May 2015, doi: 10.1093/jncimonographs/lgv021.

[42] S. Perreault *et al.*, "A phase 2 study of trametinib for patients with pediatric glioma or plexiform neurofibroma with refractory tumor and activation of the MAPK/ERK pathway: TRAM-01," *BMC Cancer*, vol. 19, no. 1, Dec. 2019, doi: 10.1186/s12885-019-6442-2.

[43] R. A. Haddad and A. N. Akansu, "A class of fast Gaussian binomial filters for speech and image processing," *IEEE Transactions on Signal Processing*, vol. 39, no. 3, pp. 723–727, Mar. 1991.

Appendix A – Supplementary figures of the article
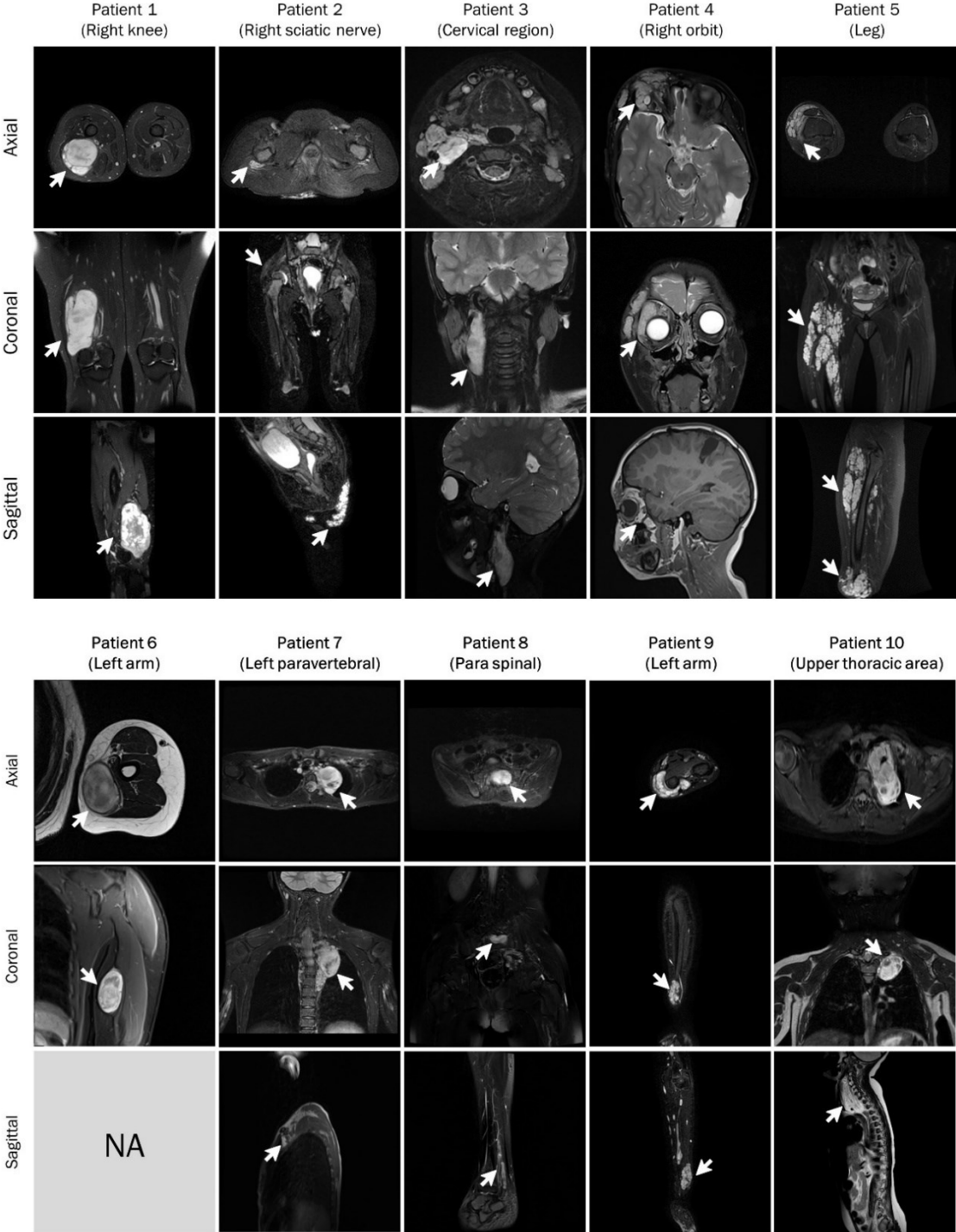
Supplementary Figure 1. MRI data of patients prescribed with either T1-, T2-, and/or STIR images in the three dimensions (except for Patient 6). Arrows indicate the location of the lesions. **NA:** Not available.

Supplementary Figure 2. A, Histogram analysis of the circular ROI drawn in B, the original MRI image. Segmentation of the lesion area using: C, SSTMean, D, SSTMini, and E, Manual tracing.